











LETTER TO THE EDITOR

# Discovery of non-metastable ammonia masers in Sagittarius B2

Y. T. Yan (闫耀庭)<sup>1,\*</sup> , C. Henkel<sup>1,2,3</sup> , K. M. Menten<sup>1</sup> , Y. Gong (龚龔)<sup>1</sup> , H. Nguyen<sup>1,\*</sup> , J. Ott<sup>4</sup> ,  
A. Ginsburg<sup>5</sup> , T. L. Wilson<sup>1</sup>, A. Brunthaler<sup>1</sup> , A. Belloche<sup>1</sup> , J. S. Zhang (张江水)<sup>6</sup> , N. Budaiev<sup>5</sup>, and D. Jeff<sup>5</sup>

<sup>1</sup> Max-Planck-Institut für Radioastronomie, Auf dem Hügel 69, 53121 Bonn, Germany

e-mail: [yyan@mpifr-bonn.mpg.de](mailto:yyan@mpifr-bonn.mpg.de), [astrotingyan@gmail.com](mailto:astrotingyan@gmail.com)

<sup>2</sup> Astronomy Department, Faculty of Science, King Abdulaziz University, P. O. Box 80203, Jeddah 21589, Saudi Arabia

<sup>3</sup> Xinjiang Astronomical Observatory, Chinese Academy of Sciences, 830011 Urumqi, PR China

<sup>4</sup> National Radio Astronomy Observatory, 520 Edgemont Road, Charlottesville, VA 22903-2475, USA

<sup>5</sup> Department of Astronomy, University of Florida, PO Box 112055, USA

<sup>6</sup> Center for Astrophysics, Guangzhou University, 510006 Guangzhou, People's Republic of China

Received 20 September; accepted 23 September

## ABSTRACT

We report the discovery of widespread maser emission in non-metastable inversion transitions of  $\text{NH}_3$  toward various parts of the Sagittarius B2 molecular cloud and star-forming region complex. We detect masers in the  $J, K = (6,3), (7,4), (8,5), (9,6),$  and  $(10,7)$  transitions toward Sgr B2(M) and Sgr B2(N), an  $\text{NH}_3 (6,3)$  maser in Sgr B2(NS), and  $\text{NH}_3 (7,4), (9,6),$  and  $(10,7)$  masers in Sgr B2(S). With the high angular resolution data of the Karl G. Jansky Very Large Array (JVLA) in the A-configuration, we identify 18 maser spots. Nine maser spots arise from Sgr B2(N), one from Sgr B2(NS), five from Sgr B2(M), and three in Sgr B2(S). Compared to our Effelsberg single-dish data, the JVLA data indicate no missing flux. The detected maser spots are not resolved by our JVLA observations. Lower limits to the brightness temperature are  $>3000$  K and reach up to several  $10^5$  K, manifesting the lines' maser nature. In view of the masers' velocity differences with respect to adjacent hot molecular cores and/or UCHII regions, it is argued that all the measured ammonia maser lines may be associated with shocks caused either by outflows or by the expansion of UCHII regions. Overall, Sgr B2 is unique in that it allows us to measure many  $\text{NH}_3$  masers simultaneously, which may be essential in order to elucidate their thus far poorly understood origin and excitation.

**Key words.** Masers – ISM: clouds – ISM: individual objects: Sgr B2 – ISM: H II regions – Radio lines: ISM

## 1. Introduction

Since their discovery in the  $(J, K) = (3,3)$  metastable ( $J = K$ ) line toward the high-mass star-forming region (HMSFR) W33 (Wilson et al. 1982), sources emitting maser emission in the ammonia molecule ( $\text{NH}_3$ ) have attracted much attention. To date, metastable ammonia maser lines have been detected in 22 HMSFRs (see Yan et al. 2022, and references therein), while non-metastable ( $J > K$ ) ammonia masers have only been found in ten sources. The  $\text{NH}_3 (6,3), (7,4), (8,5),$  and  $(9,6)$  maser lines, which will be discussed below, arise from energy levels of 551 K, 713 K, 892 K, and 1089 K above the ground state, respectively. These four maser transitions have only been detected, respectively, in three (NGC7538, W51, and Sgr B2(N)), in two (W51 and Sgr B2(N)), in two (W51 and Sgr B2(N)), and in seven (W51, NGC7538, W49, DR21 (OH), Sgr B2(N), Cep A and G34.26+0.15) HMSFRs (Madden et al. 1986; Henkel et al. 2013; Mei et al. 2020; Yan et al. 2022). The  $\text{NH}_3 (10,7)$  line, also observed by us, connects states as high as 1303 K above the ground state and has so far only been classified as a maser in W51 (Henkel et al. 2013). Among all the abovementioned re-

gions of massive star formation, Sgr B2 hosts a particularly high number of active sites of star formation.

Sgr B2 is located at a projected distance of  $\sim 100$  pc from Sgr A\* (Reid et al. 2009), the compact radio source associated with the supermassive black hole in the Galactic center at a distance of  $8.178 \pm 0.013_{\text{stat}} \pm 0.022_{\text{sys}}$  kpc (Gravity Collaboration et al. 2019). This region is normally divided into three high-mass star-forming cores: Sgr B2(N), Sgr B2(M), and Sgr B2(S) (see our Fig. 1 for the locations of these). In total, Sgr B2 contains more than 50 H II regions, most of which are ultracompact H II regions (UCH II) with diameters smaller than 0.1 pc (Gaume et al. 1995; De Pree et al. 1998, 2014, 2015; Lazio & Cordes 2008; Ginsburg et al. 2018; Meng et al. 2019, 2022; Nguyen et al. 2021). In Sgr B2 (N) and (M), several deeply embedded high-mass young stellar objects are surrounded by dense, hot molecular cores with an exceedingly rich chemistry that gives rise to a plethora of lines from numerous complex organic molecules (e.g., Belloche et al. 2008, 2013, 2022). Detected molecular maser species are OH (Gaume & Claussen 1990; Caswell et al. 2013; Cotton & Yusef-Zadeh 2016),  $\text{H}_2\text{O}$  (Reid et al. 1988; McGrath et al. 2004; Walsh et al. 2014), SiO (Morita et al. 1992; Zapata et al. 2009),  $\text{H}_2\text{CO}$  (Mehring et al. 1994; Hoffman et al. 2007; Lu et al. 2019),  $\text{CH}_3\text{OH}$  class I (Mehring et al. 1997; Cotton & Yusef-Zadeh 2016), and class II (Caswell 1996; Rickert et al. 2019; Lu et al. 2019), and  $\text{NH}_3$  (Martín-Pintado et al. 1999;

\* Member of the International Max Planck Research School (IMPRS) for Astronomy and Astrophysics at the universities of Bonn and Cologne.

Mills et al. 2018; Mei et al. 2020). In the case of  $\text{NH}_3$ , an ammonia maser in the metastable (3,3) transition was only detected in the southern part of Sgr B2(S) (Martín-Pintado et al. 1999). Another metastable ammonia maser, in the (2,2) line, was found toward SgrB2(M) (Mills et al. 2018). Recently, 18 ammonia non-metastable maser lines at frequencies of 13.0 – 24.0 GHz were detected toward Sgr B2(N) with the Shanghai 65-meter Tianma radio telescope with characteristic beam sizes of  $54 \times 18.5/\nu(\text{GHz})$  arcseconds (Mei et al. 2020).

In this letter, we report the discovery of  $\text{NH}_3$  (6,3), (7,4), (8,5), (9,6), and (10,7) masers in Sgr B2(M) and Sgr B2(N), an  $\text{NH}_3$  (6,3) maser in Sgr B2(NS), as well as  $\text{NH}_3$  (7,4), (9,6), and (10,7) masers in Sgr B2(S). All of these increase the number of (6,3), (7,4), (8,5), (9,6), and (10,7) maser detections in our Galaxy, respectively, from three to six, two to four, two to three, seven to nine, and one to four. Observations with the Effelsberg 100-meter telescope and the Karl G. Jansky Very Large Array (JVLA) are presented in Sect. 2. Results are described in Sect. 3. A comparison of the positions of the different ammonia masers with those of other relevant tracers of the interstellar medium is presented in Sect. 4. Our main results are summarized in Sect. 5.

## 2. Observations and data reduction

### 2.1. Effelsberg observations and data reduction

The  $\text{NH}_3$  (9,6) and (10,7) lines were observed toward Sgr B2 with the 100-meter Effelsberg telescope<sup>1</sup> at 12 epochs in January 2020, February and August 2021, as well as in March, May, June, July, and August 2022. The observations were performed in position switching mode. The off position was 30' in azimuth away from the source. An S14mm double beam secondary focus receiver was employed. The half power beam width (HPBW) is  $49 \times 18.5/\nu(\text{GHz})$  arcseconds, that is 49'' at 18.5 GHz, the frequency of the  $\text{NH}_3$  (9,6) line. Before August 2021, the spectrometer covered 2 GHz with a channel width of 38.1 kHz, corresponding to  $\sim 0.62 \text{ km s}^{-1}$  at 18.5 GHz. From August 2021, a high spectral resolution backend with 65536 channels and a bandwidth of 300 MHz was employed, providing a channel width of  $0.07 \text{ km s}^{-1}$  at 18.5 GHz. Pointing was checked every hour using NGC 7027. Focus calibrations were done at the beginning of the observations, and during sunset and sunrise, toward NGC 7027. The calibrator was measured between elevations of 30 and 56 degrees. The elevation on target was about 10 degrees, requiring only minimal ( $\leq 2\%$ ) elevation-dependent flux density corrections. The system temperatures were 140–220 K in a main-beam brightness temperature,  $T_{\text{MB}}$ , scale. The flux density was calibrated assuming a  $T_{\text{MB}}/S$  ratio of 1.95 K/Jy, derived from continuum cross scans of NGC 7027 (its flux density was adopted from Ott et al. 1994). Calibration uncertainties were estimated to be  $\sim 10\%$ .

We used the GILDAS/CLASS<sup>2</sup> package (Pety 2005) to reduce the spectral line data. A first-order polynomial was subtracted from each spectrum for baseline removal.

### 2.2. JVLA observations and data reduction

Observations of six  $\text{NH}_3$  lines, the (5,1), (6,3), (7,4), (8,5), (9,6), and (10,7) transitions (Table 1), toward Sgr B2 were made on 5 March 2022 with the JVLA of the National Radio Astronomy

Observatory<sup>3</sup> (NRAO) in the A-configuration (project ID: 22A-106, PI: Yaoting Yan). Eight-bit samplers were used to perform the observations. For the  $\text{NH}_3$  (9,6) and (10,7) line observations, we used two subbands with the eight-bit samplers covering a bandwidth of 16 MHz with full polarization, eight recirculations, and four baseline board pairs (BLBPs) to provide a velocity range of  $260 \text{ km s}^{-1}$  with a channel spacing of  $0.13 \text{ km s}^{-1}$ . Four additional subbands of bandwidth 16 MHz were used to cover the  $\text{NH}_3$  (5,1), (6,3), (7,4), and (8,5) lines. The remaining ten subbands of the eight-bit sampler with a bandwidth of 128 MHz were used to measure the continuum emission between 18 and 20 GHz. The primary beam of the JVLA antennas is 150'' (FWHM) at 18.5 GHz, covering all prominent star-forming regions in Sgr B2 simultaneously. 3C 286 was used as a calibrator for pointing, flux density, bandpass, and polarization (Perley & Butler 2013). J1745-2900 served as our gain calibrator during the observations. The on-source time was 30 minutes toward Sgr B2.

A total of 27 antennas were employed for the observations. Data from two antennas were lost due to technical issues. The data from the remaining 25 antennas were reduced through the Common Astronomy Software Applications package (CASA<sup>4</sup>; McMullin et al. 2007). We calibrated the data with the JVLA CASA calibration pipeline using CASA 6.2.1. The results were obtained after flagging and recalibrating data that contained artifacts. We inspected the phase, amplitude, and bandpass variations of the calibrated visibility data to search for additional artifacts before imaging. Then, the *uvcontsub* task in CASA was used to separate the calibrated visibilities into two parts: one with line-only data and the other with the line-free continuum data. The *tclean* task with a cell size of 0'02 and Briggs weighting with *robust*=0.5 was used to produce the images of spectral line and continuum emission. All of the images were corrected for primary beam response. The synthesized beams and the rms noises in a channel image for the observed lines are listed in Table 1. For the 1.6 cm (18–20 GHz) continuum emission, the synthesized beam is 0'22  $\times$  0'08 at P.A. =  $-10^\circ 61'$ . The typical absolute astrometric accuracy of the JVLA is  $\sim 10\%$  of the synthesized beam<sup>5</sup>. The flux density scale calibration accuracy is estimated to be within 15%.

The maser spots were identified in two different ways and then cross-checked. First, we searched for masers using eyes in channel maps with a velocity spacing of  $0.5 \text{ km s}^{-1}$ . Second, we used an automated source extraction code (SEC; Murugesan 2015; Nguyen 2015) running in CASA 5.4 to find the maser features. Emission with signal-to-noise ratios (S/Ns) larger than six identified in this way was considered to be a real detection. A detailed description of the SEC code can be found in Sect. 3.1 of Nguyen et al. (2022).

## 3. Results

In January 2020, with the Effelsberg 100-m telescope, we observed two strong  $\text{NH}_3$  (9,6) maser features with velocities of  $\sim 77 \text{ km s}^{-1}$  and  $\sim 84 \text{ km s}^{-1}$ , and a weaker one at  $\sim 72 \text{ km s}^{-1}$ , toward the equatorial position  $\alpha_{\text{J2000}} = 17^{\text{h}}47^{\text{m}}20^{\text{s}}.8$ , and  $\delta_{\text{J2000}} = -28^\circ 23' 32''.1$ , which is offset by  $(+3''.96, -26''.19)$  from

<sup>3</sup> The National Radio Astronomy Observatory is a facility of the National Science Foundation, operated under a cooperative agreement by Associated Universities, Inc.

<sup>4</sup> <https://casa.nrao.edu/>

<sup>5</sup> <https://science.nrao.edu/facilities/vla/docs/manuals/oss/performance-positional-accuracy>

<sup>1</sup> Based on observations with the 100-meter telescope of the MPIfR (Max-Planck-Institut für Radioastronomie) at Effelsberg.

<sup>2</sup> <https://www.iram.fr/IRAMFR/GILDAS/>

**Table 1.** Summary of the JVLA observations.

Transition ( <i>J, K</i> )	$\nu$ (GHz)	$E_{\text{low}}/k$ (K)	Baseband	Synthesized beam (arcsec)	Linear resolution (au)	P.A. (deg)	$\text{K mJy}^{-1}$	rms (mJy beam $^{-1}$ )
(5,1)	19.838346	422	A0/C0	$0.198 \times 0.085$	$1624 \times 697$	-9.807	184	3.32
(6,3)	19.757538	551	A0/C0	$0.203 \times 0.087$	$1665 \times 713$	-9.806	177	4.30
(7,4)	19.218465	713	A0/C0	$0.209 \times 0.089$	$1714 \times 730$	-9.661	178	3.85
(8,5)	18.808507	892	B0/D0	$0.214 \times 0.091$	$1755 \times 746$	-9.527	177	3.54
(9,6)	18.499390	1089	B0/D0	$0.215 \times 0.097$	$1763 \times 795$	-7.385	171	3.79
(10,7)	18.285434	1303	B0/D0	$0.220 \times 0.094$	$1804 \times 771$	-9.874	177	2.95

**Notes.** Columns (1) and (2): observed lines and corresponding rest frequencies, taken from Henkel et al. (2013). Column (3):  $E_{\text{low}}/k$ : energy above the ground state of the lower level of a given inversion doublet;  $k$  is the Boltzmann constant;  $(E_{\text{up}} - E_{\text{low}})/k \sim 1.0\text{--}1.5\text{K}$ . Column (4): baseline board pairs' setup, see details in VLA resources page. Column (5): synthesized beam. Column (6): linear resolution at a distance of 8.2 kpc. Column (7): position angle of the synthesized beam. Column (8): conversion factor from mJy to Kelvin for each transition was calculated with  $1.222 \times 10^3 / (\nu^2 \theta_{\text{maj}} \theta_{\text{min}})$ , where  $\nu$  is the frequency in units of GHz;  $\theta_{\text{maj}}$  and  $\theta_{\text{min}}$  are the major and minor axis of the synthesized beam in units of arcseconds<sup>a</sup>. Column (9): rms noise in a channel image.

<sup>a</sup> <https://science.nrao.edu/facilities/vla/proposing/TBconv>

Sgr B2(M). In addition, maser emission at  $\sim 77 \text{ km s}^{-1}$  was also found in the non-metastable para-NH<sub>3</sub> (10,7) transition. The NH<sub>3</sub> (9,6) and (10,7) maser spectra are shown in Fig. A.1. In February 2021, we extended our observations to 20 positions to cover, in a fully sampled way, an area of  $\sim 5.0$  square arc minutes surrounding Sgr B2(M) with a spacing of  $25''$ , half the beam size. (9,6) maser emission was found to be quite widespread in Sgr B2, not only residing in Sgr B2(M), but also in Sgr B2(N) and Sgr B2(S), while (10,7) masers were detected in a more limited region comprising Sgr B2(M) and Sgr B2(N). The maps of NH<sub>3</sub> (9,6) and (10,7) spectra are presented in Figs. A.2 and A.3.

Effelsberg monitoring observations spanning 19 months show that the NH<sub>3</sub> (9,6) maser at  $V_{\text{LSR}} = 72.5 \text{ km s}^{-1}$  toward Sgr B2(N) became weaker from February to August in 2021 and was not detectable from March 2022 on  $3\sigma$  levels of 0.12 Jy with a  $0.07 \text{ km s}^{-1}$  channel width. A weaker (9,6) feature at  $V_{\text{LSR}} = 63.8 \text{ km s}^{-1}$  was detected in March 2022. The (9,6) maser spectra from Sgr B2(N) are presented in Fig. A.4. NH<sub>3</sub> (9,6) line parameters obtained by Gaussian fits are listed in Table B.1. An NH<sub>3</sub> (10,7) maser was detected at a different velocity of  $82.0 \text{ km s}^{-1}$  toward Sgr B2(N). Its flux density was increasing from February to August 2021 but was decreasing from March to August 2022. In Table B.2, NH<sub>3</sub> (10,7) line parameters obtained from Gaussian fits are presented.

Toward Sgr B2(M), NH<sub>3</sub> (9,6) maser emission at  $V_{\text{LSR}} = 72.5 \text{ km s}^{-1}$  became stronger between February 2021 and March 2022, then weakened until 2022 August. Higher spectral resolution data since March 2022 show the NH<sub>3</sub> (9,6) emission to be composed of three different components. The NH<sub>3</sub> (10,7) maser in Sgr B2(M) has a velocity offset with respect to the (9,6) maser, with a velocity of  $V_{\text{LSR}} = 70.0 \text{ km s}^{-1}$ . The flux density in the Effelsberg beam remained constant within the uncertainties during the 19 months. Spectra are shown in Fig. A.5 and line parameters obtained by Gaussian fits are listed in Tables B.3 and B.4.

The 1.6 cm continuum, derived from our JVLA A-configuration measurements, is shown in Fig. 1. A total of 22 known compact H II regions (Gaume et al. 1995; De Pree et al. 1998, 2014, 2015) were detected by our observations. The locations and sizes of these sources, derived with the *imfit* task in CASA, are consistent with previous results from 7 mm continuum measurements (De Pree et al. 2015). Details are given in Table B.5.

The JVLA has a better angular resolution compared to the Effelsberg 100-m single dish and those data reveal 18 maser spots in the NH<sub>3</sub> (6,3), (7,4), (8,5), (9,6), and (10,7) transitions. We did not find any emission in the NH<sub>3</sub> (5,1) line from Sgr B2. The  $3\sigma$  upper limit for the NH<sub>3</sub> (5,1) line is  $9.96 \text{ mJy beam}^{-1}$  (about 1800 K) for a channel width of  $0.12 \text{ km s}^{-1}$ . The JVLA NH<sub>3</sub> (9,6) and (10,7) line profiles toward Sgr B2(M), extracted from an Effelsberg-beam-size region (FWHM,  $49''$ ), are shown in Fig. A.5. From the similarity of the flux density obtained at Effelsberg and the JVLA, measured in March 2022, we conclude that there is no “missing spacing” flux density in the JVLA data, that is, emission on angular scales larger than defined by the shortest JVLA baseline. NH<sub>3</sub> (6,3) masers arise from four different locations, named 63A, 63B, 63C, and 63D. NH<sub>3</sub> (7,4), (8,5), (9,6), and (10,7) masers are detected toward three, two, four, and five spots, respectively. Positions and spectral parameters of these masers are listed in Table B.6. The detected isolated maser spots are distributed over a  $16'' \times 93''$  area in Sgr B2, corresponding to  $0.6 \times 3.7 \text{ pc}$ . Details related to the individual sources are given below.

**Sgr B2(N):** Among the 18 maser spots detected in Sgr B2, 50% are located in Sgr B2(N). These are seen in the NH<sub>3</sub> (6,3) transition toward 63A and 63B, in the (7,4) transition toward 74A, in the (8,5) line toward 85A, in the (9,6) transition toward 96A and 96B, as well as in the (10,7) line toward 107A, 107B, and 107C. Four of these sources, 85A, 96A, 96B, and 107C, are close to the UCH II region K2 (see Fig. 2). The two maser spots, 85A and 107C, share the same position and have similar velocity distributions. Three maser spots, 63A, 63B, and 74A, surround the compact continuum source K3. The two maser spots, 63A and 74A, share, within the uncertainties, the same position and have similar velocity distributions. One maser spot, 107A, originates from a region offset by  $(-0'61 \pm 0'02, +0'47 \pm 0'01)$  from the continuum source K7. The second maser spot in the (10,7) line, 107B, has the highest brightness temperature. The lower limit is no less than  $6 \times 10^5 \text{ K}$  and originates from a region without any centimeter continuum source. Spectra from these nine maser spots are presented in Fig. 3.

**Sgr B2(NS):** Only one maser spot, 63C, in the NH<sub>3</sub> (6,3) transition was detected in this region. It is the strongest among all the detected (6,3) masers in Sgr B2 and is at a position with an offset of  $(-0'09 \pm 0'02, +0'01 \pm 0'01)$  from the H II region, Z10.24 (see Fig. A.6 and Table B.6). The spectrum is shown in Fig. A.7.

**Sgr B2(M):** We detected five maser spots in this area (see Fig. A.8). Three of them, 63D, 74B, and 96C, arise from similar positions close to the UCH II region F10.39. These three maser features are distributed in the same velocity range, from  $70.0 \text{ km s}^{-1}$  to  $70.4 \text{ km s}^{-1}$ , while the (6,3) maser, 63D, extends spectroscopically down to the lower velocity of  $68.0 \text{ km s}^{-1}$ . Spectra are presented in Fig. A.9. Another two maser spots, 85B and 107D, in the (8,5) and (10,7) transitions are located in regions close to the UCH II region F10.39.

**Sgr B2(S):** Three maser spots, 74C, 96D, and 107E, in the  $\text{NH}_3$  (7,4), (9,6), and (10,7) transitions, are detected in this region. These are close to each other and are found slightly off the head of the cometary UCH II source (Fig. A.10). Spectra are shown in Fig. A.11.

## 4. Discussion

As shown in Figs. A.4 and A.5, and claimed in Sect. 3, our JVLA data of  $\text{NH}_3$  (9,6) and (10,7) lines are not affected by missing flux. All of the detected maser spots are spatially unresolved, so the derived brightness temperatures are lower limits. Nevertheless, lower limits to the brightness temperature are  $>3000 \text{ K}$  and reach  $6 \times 10^5 \text{ K}$  (107B). A comparison with the  $\text{NH}_3$  (6,3), (7,4), (8,5), and (9,6) observations toward Sgr B2(N), using the TMRT 65-m telescope in March 2020 (Mei et al. 2020), reveals that almost all maser spots in our JVLA data are new detections at different velocities, with the exception of 74A. This strongly suggests substantial variations of the  $\text{NH}_3$  (6,3), (8,5), and (9,6) masers since March 2020.

Maser spots from other molecules,  $\text{H}_2\text{O}$  (McGrath et al. 2004), class II  $\text{CH}_3\text{OH}$  (Caswell 1996; Hu et al. 2016; Lu et al. 2019),  $\text{H}_2\text{CO}$  (Mehring et al. 1994; Hoffman et al. 2007; Lu et al. 2019), and OH (Gaume & Claussen 1990), are presented in Figs. 2, A.6, A.8, and A.10. The class I  $\text{CH}_3\text{OH}$  masers at 44 GHz toward the Sgr B2(M) and N regions from Mehring & Menten (1997) are outside the scales of Figs. 2, A.6, and A.8, and are therefore not shown. The SiO maser (Morita et al. 1992; Zapata et al. 2009) and the metastable  $\text{NH}_3$  (2,2) masers in Sgr B2(M) (Mills et al. 2018) originate from a region around the radio object F3, which is more than two arcseconds north of source F10.39. These sources are, therefore, also not shown in Fig. A.8. The ammonia (3,3) masers are located in an area more than 15 arcseconds south of Sgr B2(S) (Martín-Pintado et al. 1999) and outside the region shown in Fig. A.10. It is noteworthy that they are not spatially related to any (6,3) maser component, another transition within the same  $K = 3$  ladder. Our detected non-metastable  $\text{NH}_3$  masers and previously detected metastable  $\text{NH}_3$  masers arise from different regions. This indicates that these types of ammonia masers are excited in different ways.

There are no apparent space and velocity correlations between our detected non-metastable  $\text{NH}_3$  maser spots and other molecular masers. The locations of the hot cores Sgr B2(N1), N2 and N3 in Sgr B2(N), as well as Sgr B2(N5) in Sgr B2(NS), derived from the 3 mm imaging line survey "Exploring Molecular Complexity with ALMA" (EMoCA, Bonfand et al. 2017), are shown in Figs. 2 and A.6. A bipolar outflow in an east-west direction was found around the UCH II region K2, also known as Sgr B2(N1) (Higuchi et al. 2015; Bonfand et al. 2017). Bipolar outflows are also observed in a north-south direction and a northeast-southwest direction in the hot cores of Sgr B2 (N3) and N5, respectively (Bonfand et al. 2017). There is a class II  $\text{CH}_3\text{OH}$  maser spot and an  $\text{H}_2\text{O}$  maser spot close to the hot core Sgr B2(N3). Seven  $\text{NH}_3$  maser spots, 63A, 63B, 74A, 85A, 96A, 96B, and 107C, are close to the hot core Sgr B2(N1). 107A and

107B originate from regions near the hot cores Sgr B2(N2) and N3, respectively. 63C arises from an area close to the hot core Sgr B2(N5). None of the  $\text{NH}_3$  masers are spatially coincident with the hot cores in projection. The redshifts seen in 63B, 96A, and 107B, as well as blueshifts seen in 63A, 63C, 74A, 85A, 96B, 107A, and 107C with respect to the systemic velocities of the associated hot cores, may suggest that these maser spots are related to the outflows. The line profiles from these ten maser spots are shown in Figs. 3 and A.7. Bonfand et al. (2017) did not find any sign of an outflow around Sgr B2(N2), while our maser spot 107A, with a blueshifted velocity of  $V_{\text{LSR}} = 65.5 \text{ km s}^{-1}$  ( $V_{\text{sys}} = 74.0 \text{ km s}^{-1}$ ), could indicate the presence of an outflow.

All detected  $\text{NH}_3$  maser spots in Sgr B2(M) show redshifted velocities with respect to the systemic velocity of Sgr B2(M),  $V_{\text{LSR}} = 62 \text{ km s}^{-1}$  (Belloche et al. 2013). This supports the suggestion that  $\text{NH}_3$  masers in Sgr B2(M) are also related to outflows.

Toward Sgr B2(S), the ammonia maser spots 74C, 96D, and 107E also have redshifted velocities with respect to the systemic velocity of Sgr B2(S),  $V_{\text{LSR}} = 60 \text{ km s}^{-1}$  (Meng et al. 2022), which may indicate that this emission takes part in outflows. Several hot cores were identified by Jeff et al. (in prep.) in Sgr B2(S) in ALMA data (project code: 2017.1.00114.S, PI: A. Ginsburg). No hot cores were found to be close to the ammonia masers. This indicates that the presence of hot, dense gas alone is not sufficient to excite these masers. The ammonia masers detected in Sgr B2(S) are close to the head of the cometary UCH II region, similar to the  $\text{NH}_3$  (9,6) maser M1 in G34.26+0.15 (Yan et al. 2022). The maser spots in Sgr B2(S) show almost twice the angular distance compared to M1, with an offset of  $(+0'36 \pm 0'13, -0'07 \pm 0'11)$  in G34.26+0.15. In view of the different distances of G34.26+0.15 ( $D \sim 3.3 \text{ kpc}$  Yan et al. 2022) and Sgr B2 (8.2 kpc see Sect.1), the linear distance is even five times larger in Sgr B2(S), that is 0.03 pc. The velocity difference between the masers and the cometary UCH II regions is ten times higher in Sgr B2(S) than in G34.26+0.15 ( $\Delta V_{\text{SgrB2(S)}} \geq 17.4 \text{ km s}^{-1}$  and  $\Delta V_{\text{G34.26}} \sim -1.3 \text{ km s}^{-1}$ ). That indicates that the cometary UCH II region in Sgr B2(S) is more active than the one in G34.26+0.15.

Overall, the detected non-metastable ammonia masers in Sgr B2 are consistent with the discussion on pumping scenarios in Yan et al. (2022). Therefore, we speculate that the detected  $\text{NH}_3$  masers in the non-metastable (6,3), (7,4), (8,5), (9,6), and (10,7) transitions in Sgr B2(N), Sgr B2(NS), Sgr B2(M), and Sgr B2(S) appear to be associated with shocks caused either by outflows or UCH II expansion.

## 5. Summary

We report the discovery of  $\text{NH}_3$  non-metastable (6,3), (7,4), (8,5), (9,6), and (10,7) masers in Sgr B2(M) and Sgr B2(N), an  $\text{NH}_3$  (6,3) maser in Sgr B2(NS), as well as  $\text{NH}_3$  (7,4), (9,6), and (10,7) masers in Sgr B2(S). High angular resolution data from the JVLA A-configuration reveal 18 maser spots. Nine maser spots arise from Sgr B2(N), one from Sgr B2(NS), five from Sgr B2(M), and three originate in Sgr B2(S). All of these increase the number of (6,3), (7,4), (8,5), (9,6), and (10,7) maser detections in our Galaxy from three to six, two to four, two to three, seven to nine, and one to four. Compared to the Effelsberg 100-m telescope data, the JVLA data indicate no missing flux. The detected maser spots are not resolved by our JVLA observations. Lower limits to the brightness temperature are  $>3000 \text{ K}$  and reach up to  $6 \times 10^5 \text{ K}$ , manifesting their maser nature. Long-term Effelsberg monitoring (19 months) indicates that the intensities of the (9,6) masers in Sgr B2(M), as well as the (9,6) and

(10,7) masers in Sgr B2(N), show noticeable variations. However, the (10,7) maser in Sgr B2(M) is stable. While the NH<sub>3</sub> masers all arise near hot cores, there are many hot cores that do not exhibit NH<sub>3</sub> maser emission. All of these non-metastable ammonia maser lines show redshifted or blueshifted features that may be related to outflows or UCH<sub>II</sub> expansion.

*Acknowledgements.* The authors thank the anonymous referee for the useful comments that improve the manuscript. We thank Chris De Pree for providing the 7 mm continuum images of Sgr B2(M) and Sgr B2(N). Y.T.Y. is a member of the International Max Planck Research School (IMPRS) for Astronomy and Astrophysics at the Universities of Bonn and Cologne. Y.T.Y. thanks the China Scholarship Council (CSC) and the Max-Planck-Institut für Radioastronomie (MPIfR) for the financial support. Y.T.Y. also thanks his fiancée, Siqi Guo, for her support during this pandemic period. We would like to thank the staff at the Effelsberg telescope for their help provided during the observations. The National Radio Astronomy Observatory is a facility of the National Science Foundation operated under cooperative agreement by Associated Universities, Inc. We thank the staff of the JVLA, especially Tony Perreault and Drew Medlin, for their assistance with the observations and data reduction.

## References

- Belloche, A., Garrod, R. T., Zingsheim, O., Müller, H. S. P., & Menten, K. M. 2022, *A&A*, 662, A110
- Belloche, A., Menten, K. M., Comito, C., et al. 2008, *A&A*, 482, 179
- Belloche, A., Müller, H. S. P., Menten, K. M., Schilke, P., & Comito, C. 2013, *A&A*, 559, A47
- Bonfand, M., Belloche, A., Menten, K. M., Garrod, R. T., & Müller, H. S. P. 2017, *A&A*, 604, A60
- Caswell, J. L. 1996, *MNRAS*, 283, 606
- Caswell, J. L., Green, J. A., & Phillips, C. J. 2013, *MNRAS*, 431, 1180
- Cotton, W. D. & Yusef-Zadeh, F. 2016, *ApJS*, 227, 10
- De Pree, C. G., Goss, W. M., & Gaume, R. A. 1998, *ApJ*, 500, 847
- De Pree, C. G., Peters, T., Mac Low, M. M., et al. 2014, *ApJ*, 781, L36
- De Pree, C. G., Peters, T., Mac Low, M. M., et al. 2015, *ApJ*, 815, 123
- Gaume, R. A. & Claussen, M. J. 1990, *ApJ*, 351, 538
- Gaume, R. A., Claussen, M. J., de Pree, C. G., Goss, W. M., & Mehringer, D. M. 1995, *ApJ*, 449, 663
- Ginsburg, A., Bally, J., Barnes, A., et al. 2018, *ApJ*, 853, 171
- Gravity Collaboration, Abuter, R., Amorim, A., et al. 2019, *A&A*, 625, L10
- Henkel, C., Wilson, T. L., Asiri, H., & Mauersberger, R. 2013, *A&A*, 549, A90
- Higuchi, A. E., Hasegawa, T., Saigo, K., Sanhueza, P., & Chibueze, J. O. 2015, *ApJ*, 815, 106
- Hoffman, I. M., Goss, W. M., & Palmer, P. 2007, *ApJ*, 654, 971
- Hu, B., Menten, K. M., Wu, Y., et al. 2016, *ApJ*, 833, 18
- Lazio, T. J. W. & Cordes, J. M. 2008, *ApJS*, 174, 481
- Lu, X., Mills, E. A. C., Ginsburg, A., et al. 2019, *ApJS*, 244, 35
- Madden, S. C., Irvine, W. M., Matthews, H. E., Brown, R. D., & Godfrey, P. D. 1986, *ApJ*, 300, L79
- Martín-Pintado, J., Gaume, R. A., Rodríguez-Fernández, N., de Vicente, P., & Wilson, T. L. 1999, *ApJ*, 519, 667
- McGrath, E. J., Goss, W. M., & De Pree, C. G. 2004, *ApJS*, 155, 577
- McMullin, J. P., Waters, B., Schiebel, D., Young, W., & Golap, K. 2007, in *Astronomical Society of the Pacific Conference Series*, Vol. 376, *Astronomical Data Analysis Software and Systems XVI*, ed. R. A. Shaw, F. Hill, & D. J. Bell, 127
- Mehring, D. M., Goss, W. M., & Palmer, P. 1994, *ApJ*, 434, 237
- Mehring, D. M. & Menten, K. M. 1997, *ApJ*, 474, 346
- Mei, Y., Chen, X., Shen, Z.-Q., & Li, B. 2020, *ApJ*, 898, 157
- Meng, F., Sánchez-Monge, A., Schilke, P., et al. 2022, *arXiv e-prints*, arXiv:2208.07796
- Meng, F., Sánchez-Monge, A., Schilke, P., et al. 2019, *A&A*, 630, A73
- Mills, E. A. C., Ginsburg, A., Clements, A. R., et al. 2018, *ApJ*, 869, L14
- Morita, K.-I., Hasegawa, T., Ukita, N., Okumura, S. K., & Ishiguro, M. 1992, *PASJ*, 44, 373
- Murugesan. 2015, Master's thesis, University of Bonn
- Nguyen. 2015, Master's thesis, University of Bonn
- Nguyen, H., Rugel, M. R., Menten, K. M., et al. 2021, *A&A*, 651, A88
- Nguyen, H., Rugel, M. R., Murugesan, C., et al. 2022, *arXiv e-prints*, arXiv:2207.10548
- Ott, M., Witzel, A., Quirrenbach, A., et al. 1994, *A&A*, 284, 331
- Perley, R. A. & Butler, B. J. 2013, *ApJS*, 204, 19
- Pety, J. 2005, in *SF2A-2005: Semaine de l'Astrophysique Française*, ed. F. Casoli, T. Contini, J. M. Hameury, & L. Pagani, 721
- Reid, M. J., Menten, K. M., Zheng, X. W., Brunthaler, A., & Xu, Y. 2009, *ApJ*, 705, 1548
- Reid, M. J., Schneps, M. H., Moran, J. M., et al. 1988, *ApJ*, 330, 809
- Rickert, M., Yusef-Zadeh, F., & Ott, J. 2019, *MNRAS*, 482, 5349
- Walsh, A. J., Purcell, C. R., Longmore, S. N., et al. 2014, *MNRAS*, 442, 2240
- Wilson, T. L., Batrla, W., & Pauls, T. A. 1982, *A&A*, 110, L20
- Yan, Y. T., Henkel, C., Menten, K. M., et al. 2022, *A&A*, 659, A5
- Zapata, L. A., Menten, K., Reid, M., & Beuther, H. 2009, *ApJ*, 691, 332

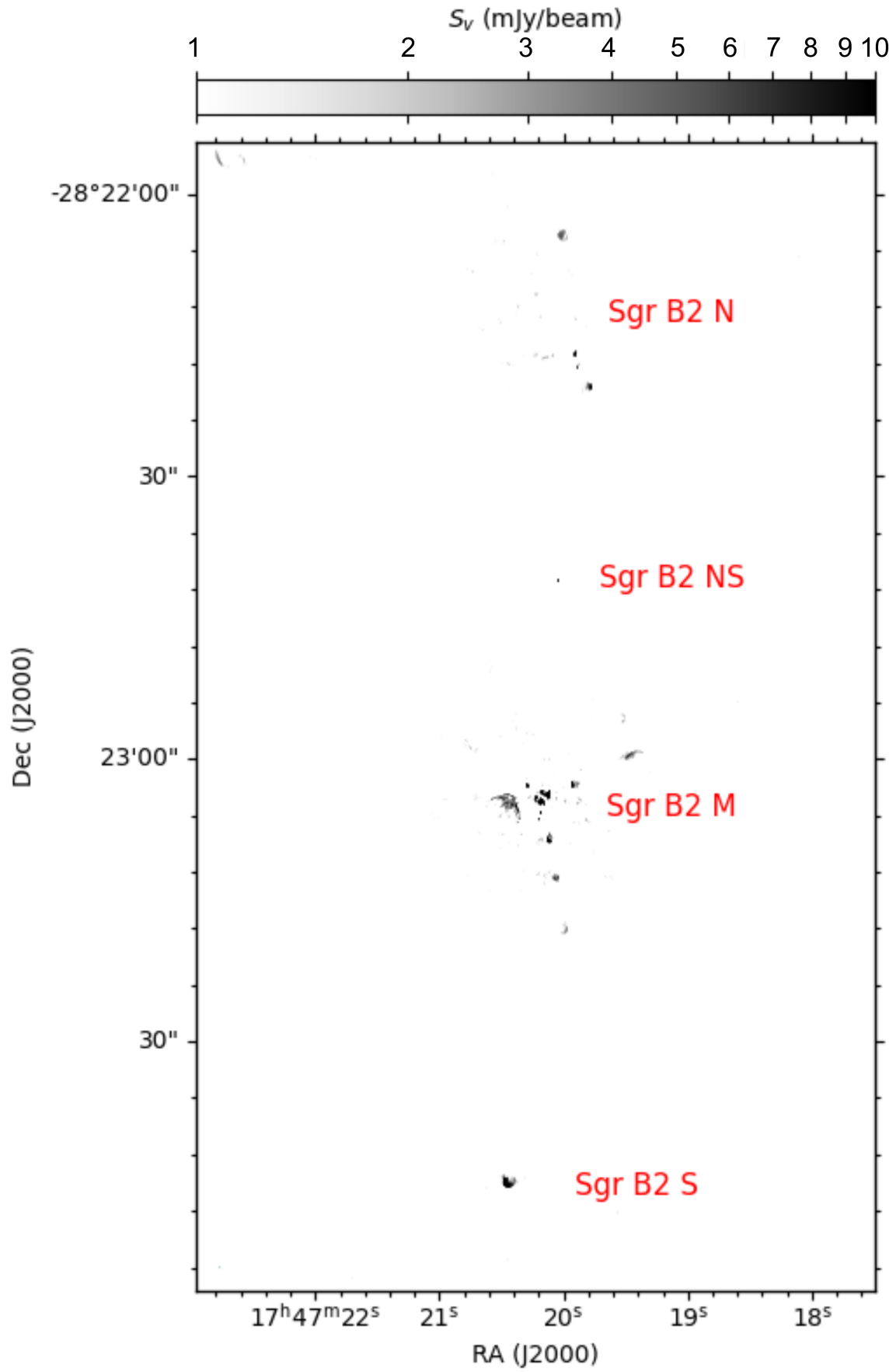


**Fig. 1.** JVLA 1.6-cm continuum map of Sgr B2, shown in gray. The synthesized beam is  $0''.22 \times 0''.08$ , P.A. =  $-10^{\circ}61$ .

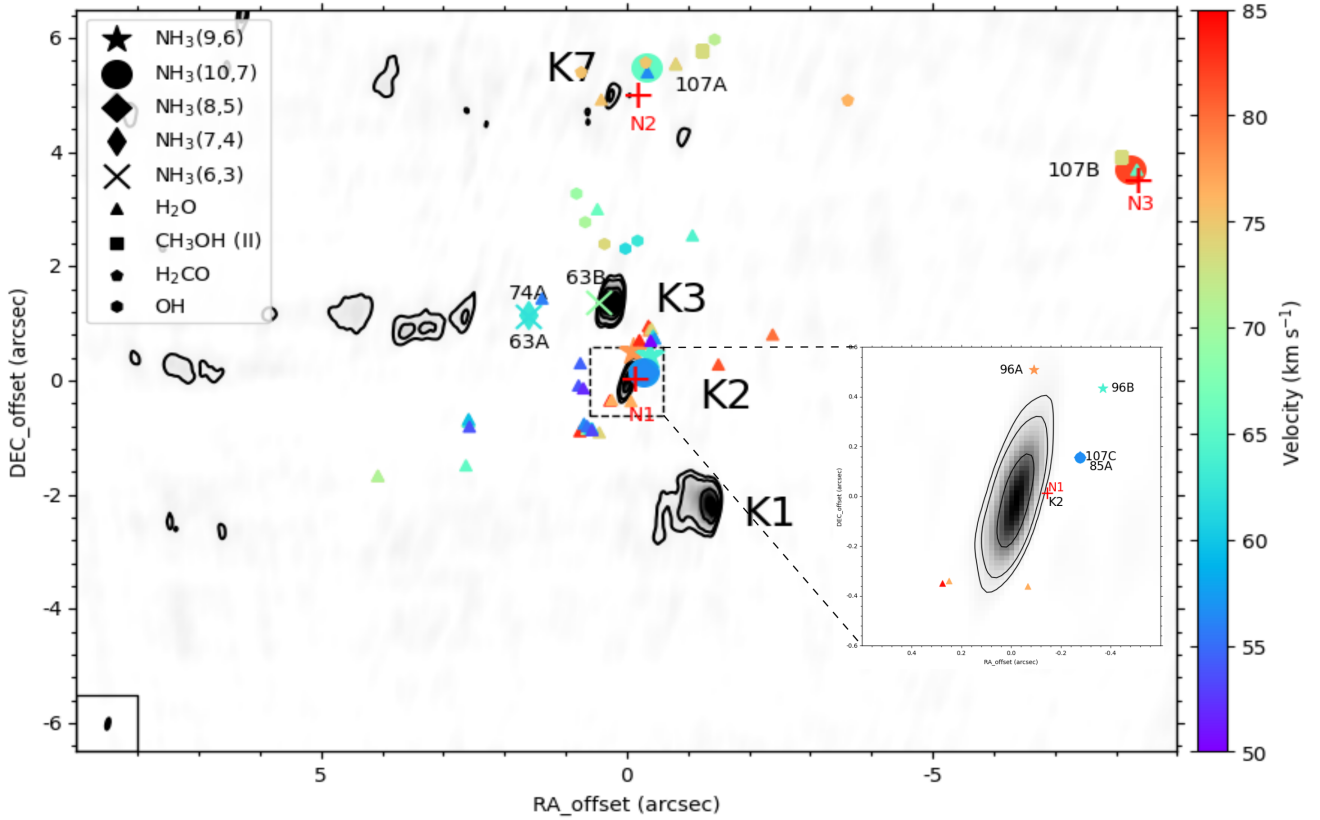


**Fig. 2.** JVL A 1.6 cm continuum map of Sgr B2(N), shown by the gray shaded areas and black contours with levels of  $5, 10, 30,$  and  $50 \times 0.2$  mJy beam $^{-1}$ . The reference position is  $\alpha_{J2000} = 17^{\text{h}}47^{\text{m}}19^{\text{s}}.883$ , and  $\delta_{J2000} = -28^{\circ}22'18''.412$ , the peak position of the continuum source K2. The crosses, thin diamonds, diamonds, stars, and circles show the positions of NH $_3$  (6,3), (7,4), (8,5), (9,6), and (10,7) emissions. H $_2$ O (McGrath et al. 2004), class II CH $_3$ OH (Caswell 1996; Lu et al. 2019), H $_2$ CO (Mehring et al. 1994; Hoffman et al. 2007; Lu et al. 2019), and OH (Gaume & Claussen 1990) masers are presented as triangles, squares, pentagons, and hexagons, respectively. The color bar indicates the velocity range ( $V_{\text{LSR}}$ ) of maser spots. Red crosses mark the positions of the hot cores Sgr B2(N1), N2, and N3, taken from the 3 mm imaging line survey "Exploring Molecular Complexity with ALMA" (EMoCA, Bonfand et al. 2017). The systemic velocities of the hot cores N1, N2, and N3 are  $V_{\text{LSR}} = 64$  km s $^{-1}$ ,  $V_{\text{LSR}} = 74$  km s $^{-1}$  and  $V_{\text{LSR}} = 74$  km s $^{-1}$ , respectively (Bonfand et al. 2017).

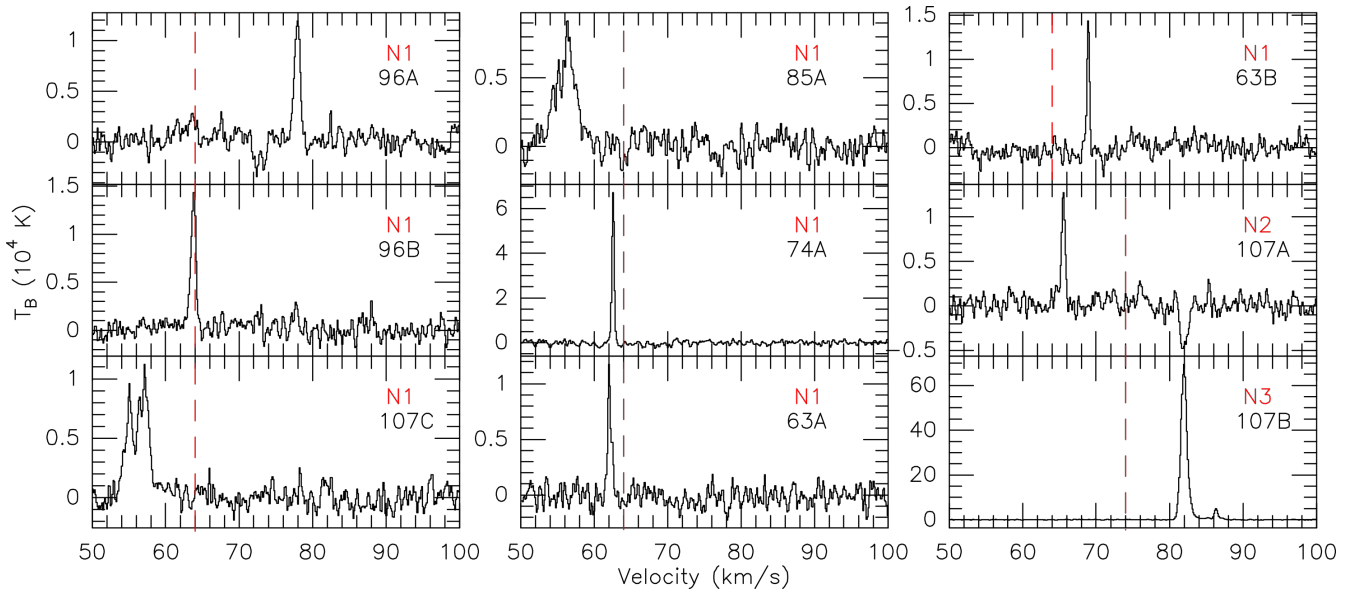


**Fig. 3.** JVL A A-configuration spectra of NH $_3$  transition lines toward Sgr B2(N). The dashed red lines indicate the systemic velocities of the associated hot cores.  $V_{\text{LSR}} = 64$  km s $^{-1}$  for N1, and  $V_{\text{LSR}} = 74$  km s $^{-1}$  for N2 and N3 (Bonfand et al. 2017). Main beam brightness temperature scales are presented on the left hand side of the profiles.

## Appendix A: Figures

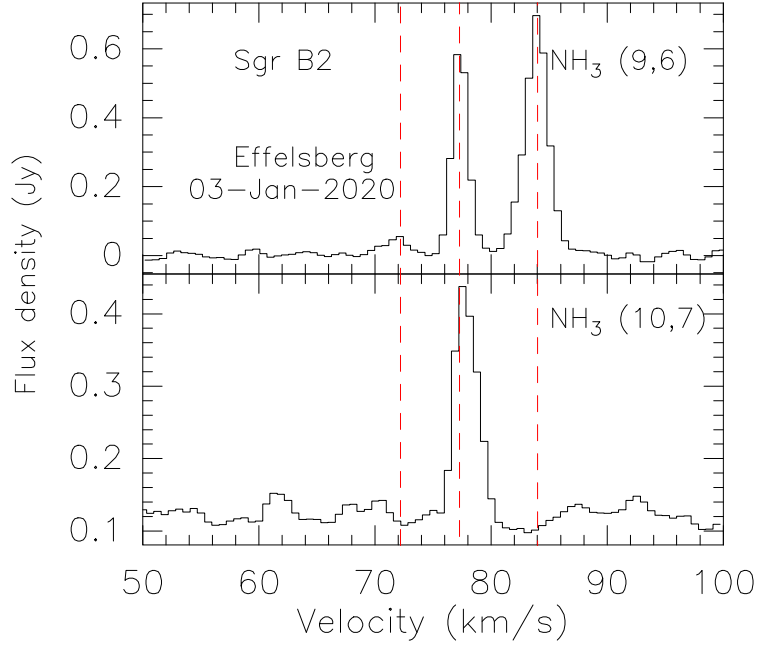


**Fig. A.1.**  $\text{NH}_3$  (9,6) and (10,7) maser lines from the 100-m telescope at Effelsberg toward a region south of Sgr B2(M), at  $\alpha_{J2000} = 17^{\text{h}}47^{\text{m}}20^{\text{s}}.8$ ,  $\delta_{J2000} = -28^{\circ}23'32''.1$ . The three red dashed lines indicate the three different velocity components at  $V_{\text{LSR}} = \sim 72 \text{ km s}^{-1}$ ,  $\sim 77 \text{ km s}^{-1}$ , and  $\sim 84 \text{ km s}^{-1}$ .

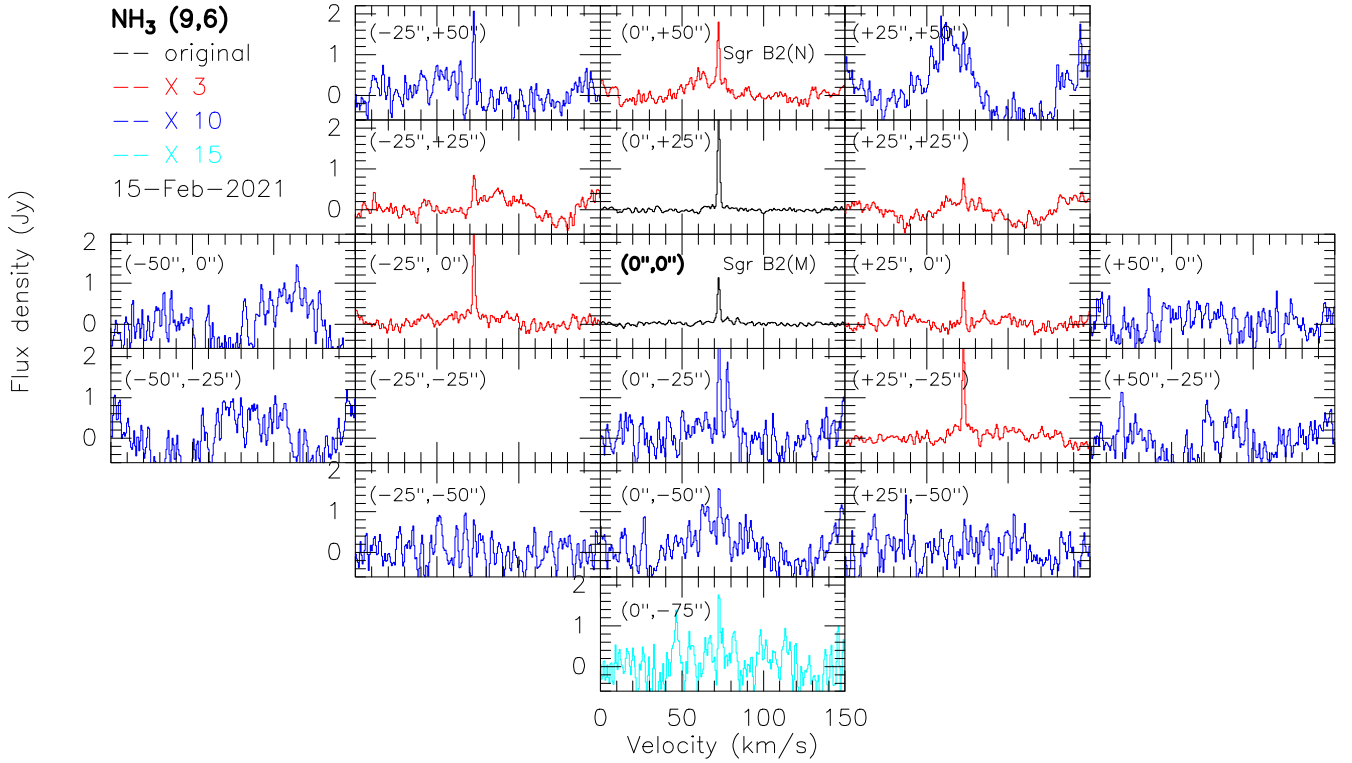


**Fig. A.2.**  $\text{NH}_3$  (9,6) line profiles observed with the Effelsberg 100-m telescope over the region of Sgr B2. The black spectra show the original flux density scales. The red, blue, and cyan spectra are presented after multiplying the flux densities by factors of three, ten, and fifteen, respectively.



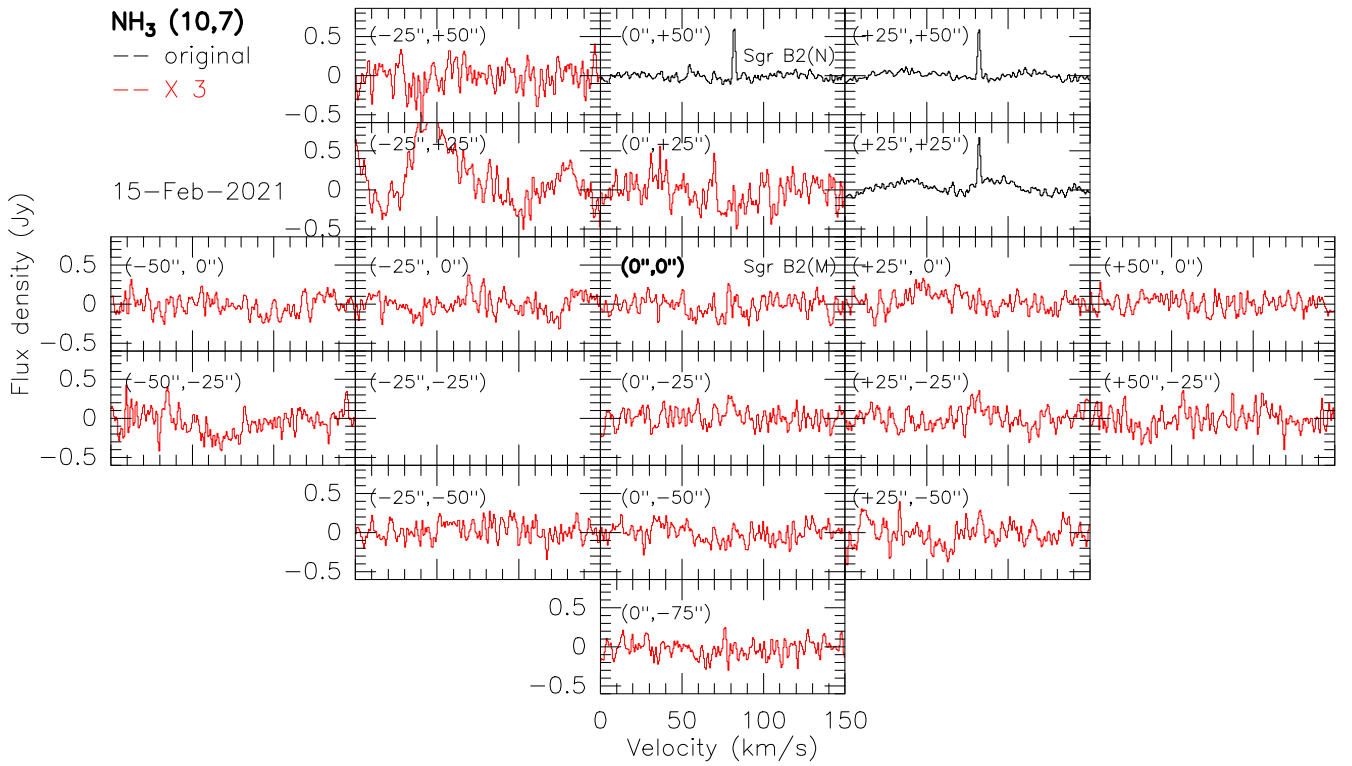


**Fig. A.3.**  $\text{NH}_3$  (10,7) spectra observed with the Effelsberg 100-m telescope toward Sgr B2. The black spectra show the original flux density scales, while the red spectra are presented after multiplying the flux densities by a factor of three.

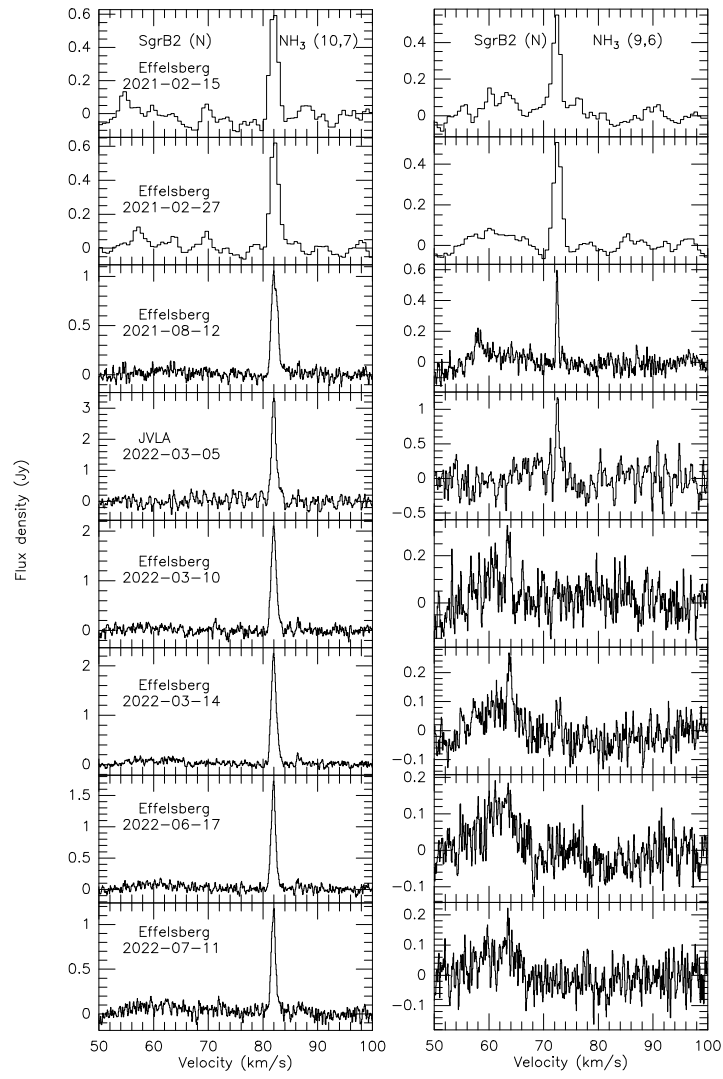


**Fig. A.4.** Effelsberg 100-meter telescope and JVL A A-configuration spectra from  $\text{NH}_3$  (9,6) and (10,7) transition lines at eight epochs toward Sgr B2(N), after subtracting a first-order polynomial baseline. The JVL A spectra are extracted over a region of radius  $35''$  centered at Sgr B2(N).

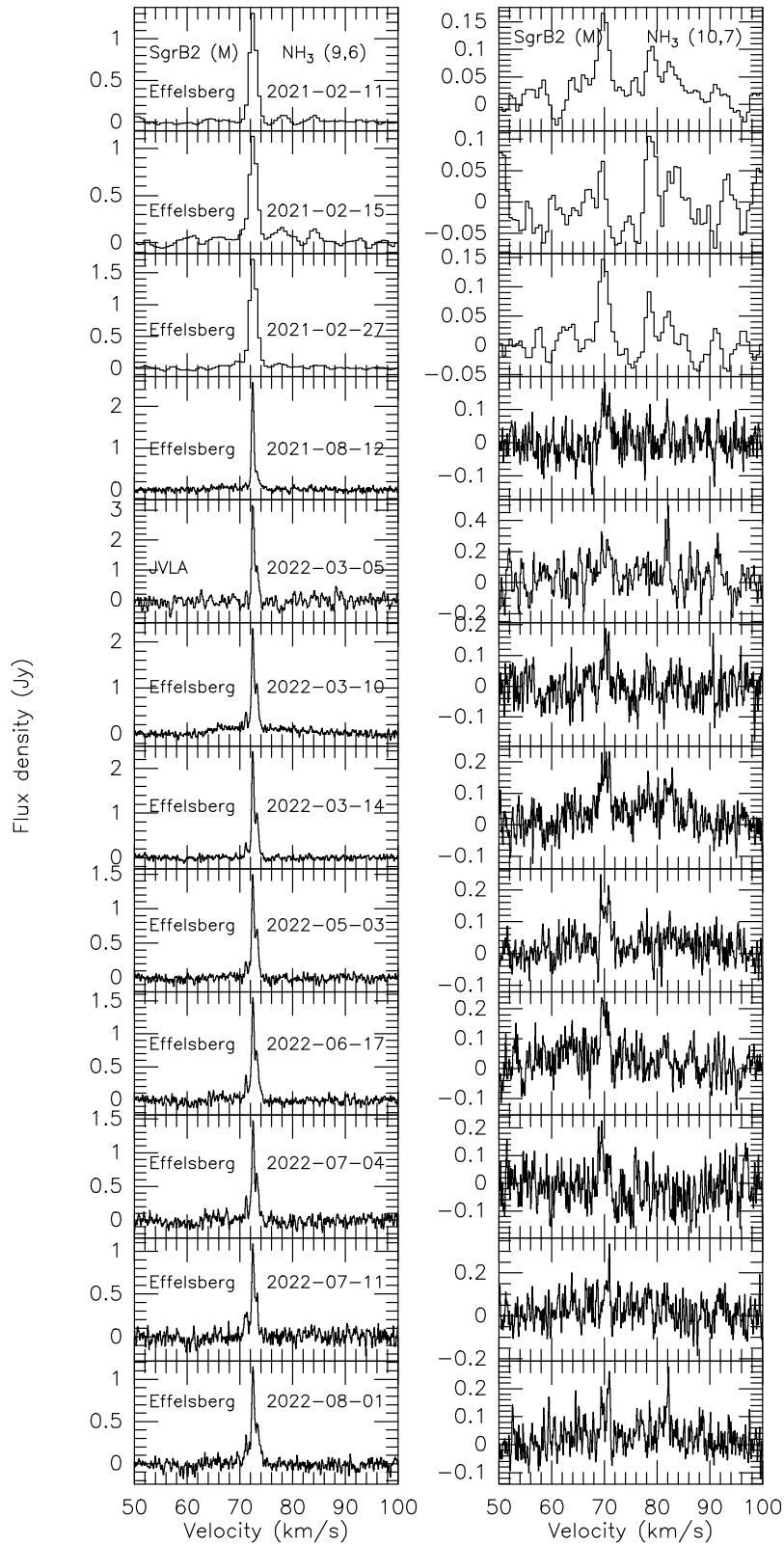


**Fig. A.5.** Effelsberg 100-meter telescope and JVLA A-configuration spectra from  $\text{NH}_3$  (9,6) and (10,7) transition lines at 12 epochs toward Sgr B2(M), after subtracting a first-order polynomial baseline. The JVLA spectra are extracted from the Effelsberg beam (FWHM,  $49''$ ) sized region.

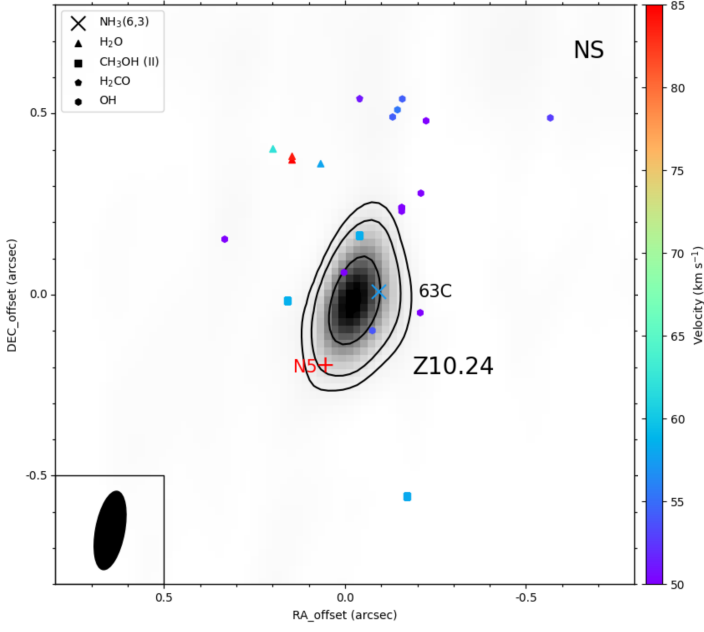


**Fig. A.6.** JVLA 1.6 cm continuum map of Sgr B2(NS) presented as gray shaded area and black contours with levels of 5, 10, 30, and  $50 \times 0.2$  mJy beam $^{-1}$ . The reference position is  $\alpha_{J2000} = 17^{\text{h}}47^{\text{m}}20^{\text{s}}.043$ , and  $\delta_{J2000} = -28^{\circ}22'41''.143$ , the peak position of continuum source Z10.24. The yellow cross shows the position of NH $_3$  (6,3) emission. H $_2$ O (McGrath et al. 2004), class II CH $_3$ OH (Caswell 1996; Hu et al. 2016; Lu et al. 2019), H $_2$ CO (Hoffman et al. 2007), and OH (Gaume & Claussen 1990) masers are presented as triangles, squares, pentagons, and hexagons, respectively. The color bar indicates the velocity range ( $V_{\text{LSR}}$ ) of the maser spots. The red cross marks the position of the hot core, Sgr B2(N5), taken from the 3 mm imaging line survey EMOCA (Bonfand et al. 2017). The systemic velocity of the hot core, N5, is  $V_{\text{LSR}} = 60$  km s $^{-1}$  (Bonfand et al. 2017).

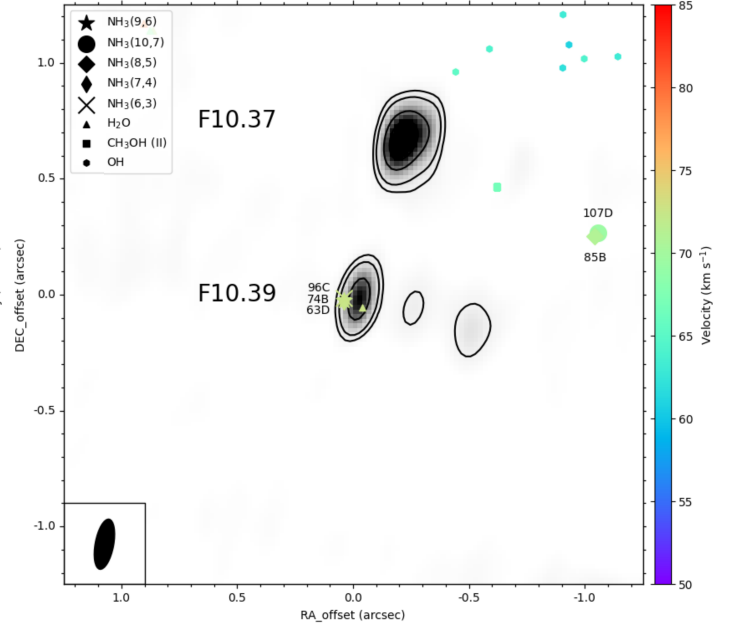


**Fig. A.8.** JVLA 1.6 cm continuum map of Sgr B2(M) presented as gray shaded areas and black contours with levels of 5, 10, 30, and  $50 \times 0.2$  mJy beam $^{-1}$ . The reference position is  $\alpha_{J2000} = 17^{\text{h}}47^{\text{m}}20^{\text{s}}.197$ , and  $\delta_{J2000} = -28^{\circ}23'06''.484$ , the peak position of continuum source F10.39. The cross, thin diamond, diamond, circle and star show the positions of NH $_3$  (6,3), (7,4), (8,5), (9,6), and (10,7) emissions. H $_2$ O (McGrath et al. 2004), class II CH $_3$ OH (Lu et al. 2019), and OH (Gaume & Claussen 1990) masers are presented as triangles, squares, and hexagons, respectively. The color bar indicates the velocity range ( $V_{\text{LSR}}$ ) of the maser spots. The systemic velocity of Sgr B2(M) is  $V_{\text{LSR}} = 62$  km s $^{-1}$  (Belloche et al. 2013).

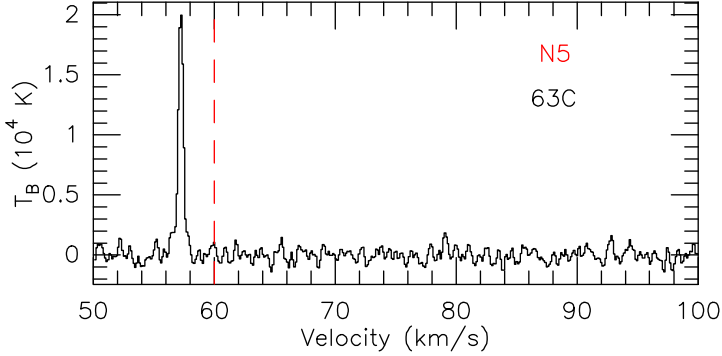


**Fig. A.7.** JVLA A-configuration spectrum of the NH $_3$  (6,3) transition line toward Sgr B2(NS). The systemic velocity of the associated hot core,  $V_{\text{LSR}} = 60$  km s $^{-1}$  in N5 (Bonfand et al. 2017), is indicated by the dashed red line.

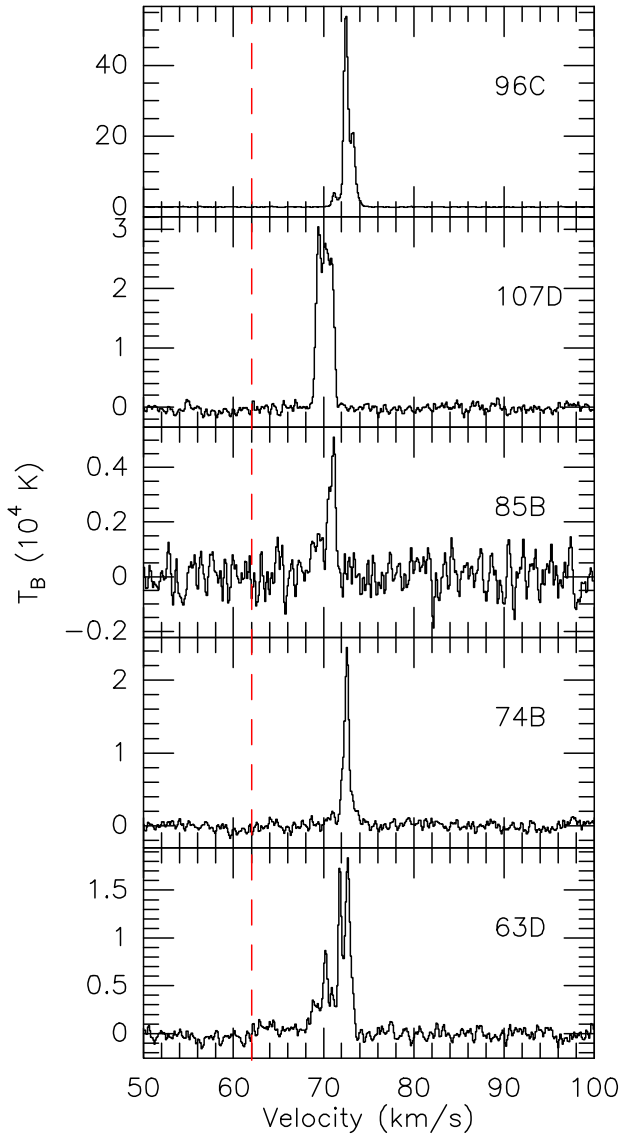


**Fig. A.9.** JVL A-configuration spectra of  $\text{NH}_3$  transition lines toward Sgr B2(M). The systemic velocity of Sgr B2(M),  $V_{\text{LSR}} = 62 \text{ km s}^{-1}$  (Belloche et al. 2013), is indicated by the dashed red line.

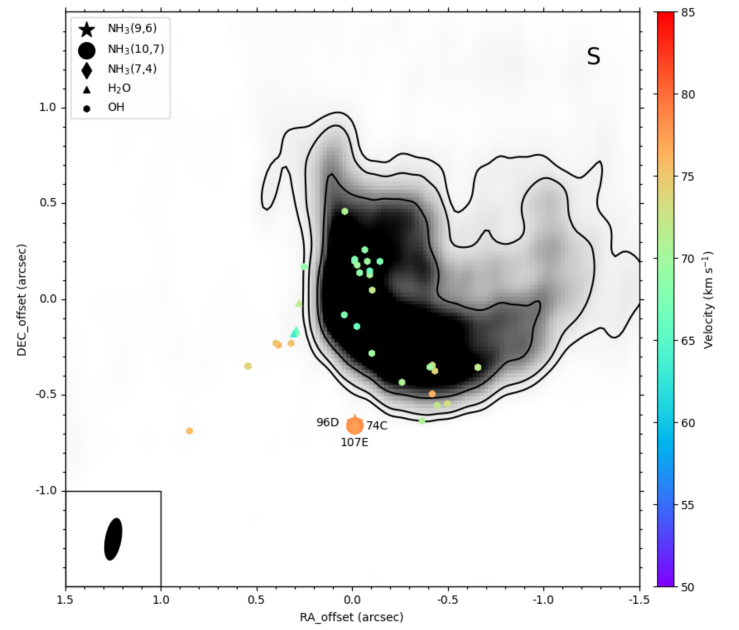


**Fig. A.10.** JVL 1.6 cm continuum map of Sgr B2(S) presented as gray shaded areas and black contours with levels of 5, 10, 30, and  $50 \times 0.2 \text{ mJy beam}^{-1}$ . The reference position is  $\alpha_{J2000} = 17^{\text{h}}47^{\text{m}}20^{\text{s}}.472$ , and  $\delta_{J2000} = -28^{\circ}23'45''.120$ , the peak position of the continuum source. The thin diamond, star, and circle show the positions of  $\text{NH}_3$  (7,4), (9,6), and (10,7) emissions.  $\text{H}_2\text{O}$  (McGrath et al. 2004) and OH (Gaume & Claussen 1990) masers are presented as triangles and hexagons, respectively. The color bar indicates the velocity range ( $V_{\text{LSR}}$ ) of the maser spots. The systemic velocity of Sgr B2(S) is  $V_{\text{LSR}} = 60 \text{ km s}^{-1}$  (Meng et al. 2022).

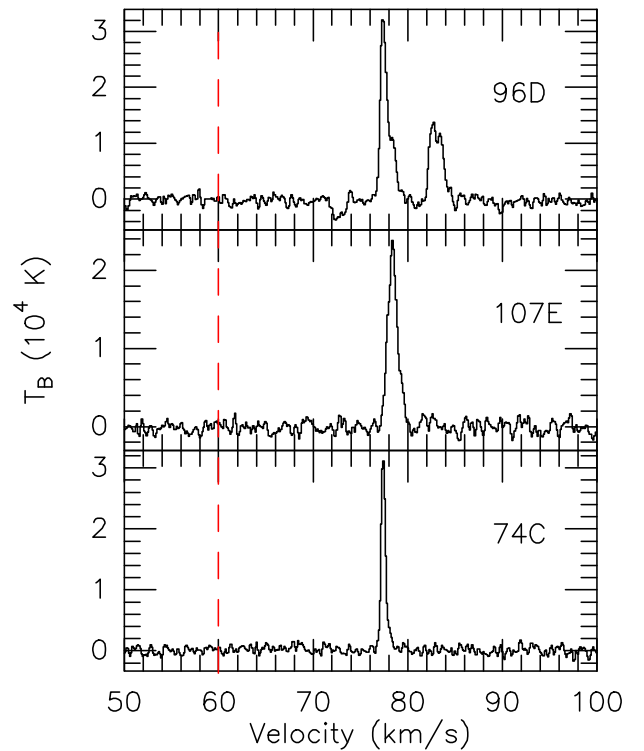


**Fig. A.11.** JVL A-configuration spectra of  $\text{NH}_3$  transition lines toward Sgr B2(S). The systemic velocity of Sgr B2(S),  $V_{\text{LSR}} = 60 \text{ km s}^{-1}$  (Meng et al. 2022), is indicated by the dashed red line.

## Appendix B: Tables

**Table B.1.** Summary of NH<sub>3</sub> (9,6) maser observations toward Sgr B2(N)

Source	Telescope	Beam size	Epoch	Channel spacing (km s <sup>-1</sup> )	$S_\nu$ (Jy)	rms (Jy)	$\int S_\nu d\nu$ (Jy km s <sup>-1</sup> )	$V_{\text{LSR}}$ (km s <sup>-1</sup> )	$\Delta V_{1/2}$ (km s <sup>-1</sup> )	
Sgr B2(N)	Effelsberg	49''	2021, Feb. 15	0.62	0.53	0.034	1.03 ± 0.09	72.34 ± 0.07	1.83 ± 0.21	
	Effelsberg	49''	2021, Feb. 27	0.62	0.52	0.028	0.92 ± 0.06	72.54 ± 0.05	1.65 ± 0.12	
	Effelsberg	49''	2021, Aug. 12	0.07	0.09	0.043	1.16 ± 0.09	63.02 ± 0.50	12.14 ± 0.88	
							0.14	0.34 ± 0.06	58.09 ± 0.09	2.17 ± 0.39
							0.61	0.30 ± 0.01	72.48 ± 0.01	0.47 ± 0.02
	JVLA <sup>a</sup>	0'':215 × 0'':097	2022, Mar. 05	0.13	1.16	0.189	0.89 ± 0.09	72.55 ± 0.04	0.72 ± 0.10	
	Effelsberg	49''	2022, Mar. 10	0.07	0.30	0.067	0.32 ± 0.03	63.52 ± 0.05	1.01 ± 0.12	
	Effelsberg	49''	2022, Mar. 14	0.07	0.12	0.041	1.37 ± 0.06	60.99 ± 0.22	10.29 ± 0.47	
							0.20	0.16 ± 0.02	63.81 ± 0.04	0.79 ± 0.09
							0.10	0.12 ± 0.02	72.66 ± 0.09	1.12 ± 0.15
	Effelsberg	49''	2022, Jun. 17	0.07	...	0.041	...	...	...	
	Effelsberg	49''	2022, Jul. 11	0.07	...	0.047	...	...	...	

**Notes.** The spectral parameters are obtained from Gaussian-fitting. <sup>(a)</sup> The JVLA spectrum is extracted from a region of radius 35''.

**Table B.2.** Summary of NH<sub>3</sub> (10,7) maser observations toward Sgr B2(N)

Source	Telescope	Beam size	Epoch	Channel spacing (km s <sup>-1</sup> )	$S_\nu$ (Jy)	rms (Jy)	$\int S_\nu d\nu$ (Jy km s <sup>-1</sup> )	$V_{\text{LSR}}$ (km s <sup>-1</sup> )	$\Delta V_{1/2}$ (km s <sup>-1</sup> )
Sgr B2(N)	Effelsberg	49''	2021, Feb. 15	0.62	0.66	0.048	1.12 ± 0.07	81.99 ± 0.05	1.60 ± 0.11
	Effelsberg	49''	2021, Feb. 27	0.62	0.64	0.038	1.19 ± 0.06	82.10 ± 0.04	1.76 ± 0.10
	Effelsberg	49''	2021, Aug. 12	0.07	1.02	0.045	1.44 ± 0.02	82.10 ± 0.01	1.33 ± 0.02
	JVLA <sup>a</sup>	0'':220 × 0'':094	2022, Mar. 05	0.13	3.21	0.141	3.49 ± 0.09	81.99 ± 0.01	1.02 ± 0.03
	Effelsberg	49''	2022, Mar. 10	0.07	2.02	0.070	2.35 ± 0.03	81.97 ± 0.01	1.09 ± 0.02
	Effelsberg	49''	2022, Mar. 14	0.07	2.12	0.051	2.48 ± 0.02	81.96 ± 0.01	1.10 ± 0.01
	Effelsberg	49''	2022, Jun. 17	0.07	1.61	0.051	1.66 ± 0.02	81.90 ± 0.01	0.97 ± 0.02
	Effelsberg	49''	2022, Jul. 11	0.07	1.11	0.055	1.13 ± 0.03	81.91 ± 0.01	0.96 ± 0.03

**Notes.** The spectral parameters are obtained from Gaussian-fitting. <sup>(a)</sup> The JVLA spectrum is extracted from a region of radius 35''.

**Table B.3.** Summary of NH<sub>3</sub> (9,6) maser observations toward Sgr B2(M)

Source	Telescope	Beam size	Epoch	Channel spacing (km s <sup>-1</sup> )	$S_\nu$ (Jy)	rms (Jy)	$\int S_\nu dv$ (Jy km s <sup>-1</sup> )	$V_{\text{LSR}}$ (km s <sup>-1</sup> )	$\Delta V_{1/2}$
Sgr B2(M)	Effelsberg	49''	2021, Feb. 11	0.62	1.29	0.021	2.22 ± 0.03	72.49 ± 0.01	1.61 ± 0.03
					0.09		0.17 ± 0.03	78.23 ± 0.17	1.76 ± 0.32
Effelsberg	49''	2021, Feb. 15	0.62	0.08	0.035	2.13 ± 0.06	72.52 ± 0.02	1.82 ± 0.06	
				0.15		0.59 ± 0.08	77.83 ± 0.25	3.78 ± 0.59	
				0.15		0.30 ± 0.06	84.18 ± 0.19	1.84 ± 0.40	
Effelsberg	49''	2021, Feb. 27	0.62	1.69	0.018	3.06 ± 0.05	72.53 ± 0.01	1.70 ± 0.03	
Effelsberg	49''	2021, Aug. 12	0.07	2.30	0.040	1.17 ± 0.03	72.47 ± 0.01	0.48 ± 0.01	
JVLA <sup>a</sup>	0'':215 × 0'':097	2022, Mar. 05	0.13	0.39	0.154	0.80 ± 0.04	72.92 ± 0.04	1.92 ± 0.11	
				3.20		1.71 ± 0.15	72.45 ± 0.02	0.50 ± 0.03	
Effelsberg	49''	2022, Mar. 10	0.07	1.11	0.048	0.99 ± 0.16	73.19 ± 0.07	0.84 ± 0.13	
				0.39		0.33 ± 0.02	71.22 ± 0.07	0.80 ± 0.07	
Effelsberg	49''	2022, Mar. 14	0.07	2.16	0.040	1.31 ± 0.02	72.45 ± 0.07	0.57 ± 0.07	
				1.00		0.91 ± 0.02	73.27 ± 0.07	0.85 ± 0.07	
				0.26		0.21 ± 0.02	71.26 ± 0.03	0.76 ± 0.07	
Effelsberg	49''	2022, May. 03	0.07	2.38	0.037	1.25 ± 0.02	72.46 ± 0.01	0.49 ± 0.01	
				0.97		0.77 ± 0.02	73.26 ± 0.01	0.74 ± 0.03	
				0.18		0.20 ± 0.02	71.36 ± 0.06	1.01 ± 0.12	
Effelsberg	49''	2022, Jun. 17	0.07	1.45	0.044	0.78 ± 0.03	72.47 ± 0.01	0.51 ± 0.02	
				0.70		0.56 ± 0.03	73.25 ± 0.02	0.75 ± 0.04	
				0.28		0.25 ± 0.01	71.27 ± 0.07	0.84 ± 0.07	
Effelsberg	49''	2022, Jul. 04	0.07	1.47	0.058	0.88 ± 0.01	72.48 ± 0.07	0.56 ± 0.07	
				0.68		0.58 ± 0.01	73.27 ± 0.07	0.80 ± 0.07	
				0.38		0.18 ± 0.01	71.22 ± 0.07	0.45 ± 0.07	
Effelsberg	49''	2022, Jul. 11	0.07	1.43	0.064	0.89 ± 0.01	72.52 ± 0.07	0.58 ± 0.07	
				0.67		0.43 ± 0.01	73.32 ± 0.07	0.60 ± 0.07	
				0.28		0.25 ± 0.02	71.21 ± 0.04	0.84 ± 0.08	
Effelsberg	49''	2022, Aug. 01	0.07	1.04	0.049	0.62 ± 0.03	72.51 ± 0.01	0.56 ± 0.04	
				0.48		0.28 ± 0.03	73.23 ± 0.03	0.55 ± 0.07	
				0.25		0.13 ± 0.03	71.14 ± 0.03	0.50 ± 0.13	
Effelsberg	49''	2022, Aug. 01	0.07	0.77	0.049	0.35 ± 0.02	72.50 ± 0.01	0.42 ± 0.02	
				0.48		1.00 ± 0.05	72.93 ± 0.04	1.96 ± 0.10	

**Notes.** The spectral parameters are obtained from Gaussian-fitting. <sup>(a)</sup> The JVLA spectrum toward Sgr B2(M) is extracted from the Effelsberg beam (FWHM, 49'') sized region.

**Table B.4.** Summary of NH<sub>3</sub> (10,7) maser observations toward Sgr B2(M)

Source	Telescope	Beam size	Epoch	Channel spacing (km s <sup>-1</sup> )	$S_\nu$ (Jy)	rms (Jy)	$\int S_\nu dv$ (Jy km s <sup>-1</sup> )	$V_{\text{LSR}}$ (km s <sup>-1</sup> )	$\Delta V_{1/2}$
Sgr B2(M)	Effelsberg	49''	2021, Feb. 11	0.62	0.15	0.020	0.38 ± 0.06	69.77 ± 0.19	2.46 ± 0.47
	Effelsberg	49''	2021, Feb. 15	0.62	...	0.032	...	...	...
	Effelsberg	49''	2021, Feb. 27	0.62	0.15	0.021	0.33 ± 0.05	69.86 ± 0.14	2.09 ± 0.32
	Effelsberg	49''	2021, Aug. 12	0.07	0.14	0.041	0.08 ± 0.02	69.59 ± 0.05	0.51 ± 0.17
					0.14		0.03 ± 0.02	70.07 ± 0.03	0.18 ± 0.09
					0.10		0.13 ± 0.04	70.80 ± 0.12	1.22 ± 0.59
	JVLA <sup>a</sup>	0''.220 × 0''.094	2022, Mar. 05	0.13	0.35	0.127	0.22 ± 0.06	69.55 ± 0.07	0.58 ± 0.22
					0.71		0.76 ± 0.06	81.90 ± 0.04	1.01 ± 0.09
	Effelsberg	49''	2022, Mar. 10	0.07	0.14	0.049	0.16 ± 0.03	70.10 ± 0.08	1.08 ± 0.25
					0.16		0.04 ± 0.01	70.80 ± 0.03	0.25 ± 0.06
	Effelsberg	49''	2022, Mar. 14	0.07	0.16	0.043	0.51 ± 0.04	70.13 ± 0.11	3.02 ± 0.37
	Effelsberg	49''	2022, May. 03	0.07	0.17	0.039	0.04 ± 0.02	69.26 ± 0.02	0.23 ± 0.09
					0.11		0.07 ± 0.03	69.62 ± 0.17	0.65 ± 0.18
					0.15		0.21 ± 0.05	70.72 ± 0.11	1.28 ± 0.33
	Effelsberg	49''	2022, Jun. 17	0.07	0.20	0.051	0.15 ± 0.05	69.53 ± 0.09	0.70 ± 0.22
					0.16		0.17 ± 0.05	70.48 ± 0.16	0.99 ± 0.25
	Effelsberg	49''	2022, Jul. 04	0.07	0.17	0.063	0.22 ± 0.04	69.39 ± 0.09	1.21 ± 0.30
	Effelsberg	49''	2022, Jul. 11	0.07	0.14	0.060	0.14 ± 0.03	70.30 ± 0.11	0.97 ± 0.22
					0.28		0.07 ± 0.02	70.92 ± 0.02	0.22 ± 0.06
	Effelsberg	49''	2022, Aug. 01	0.07	0.15	0.048	0.13 ± 0.01	69.54 ± 0.08	0.79 ± 0.08
				0.25		0.14 ± 0.01	70.81 ± 0.08	0.54 ± 0.08	
				0.07		0.24 ± 0.01	81.52 ± 0.08	3.15 ± 0.08	
				0.19		0.06 ± 0.01	82.10 ± 0.08	0.31 ± 0.08	

**Notes.** The spectral parameters are obtained from Gaussian-fitting. <sup>(a)</sup> The JVLA spectrum toward Sgr B2(M) is extracted from the Effelsberg beam (FWHM, 49'') sized region.

**Table B.5.** 1.6 cm JVLA flux densities of individual continuum sources

Source	R.A. (h m s)	Dec. (° ' ")	Deconvolved Size (arcsec)	P.A. (deg)	$S_\nu$ (mJy)	
Sgr B2	B	17 47 19.927 ± 0.019	-28 23 02.832 ± 0.041	(0.796 ± 0.105) × (0.331 ± 0.046)	15.6	181 ± 22
	B10.06	17 47 19.864 ± 0.010	-28 23 01.247 ± 0.013	(~0.22) × (~0.12)		6 ± 1
	E	17 47 20.116 ± 0.013	-28 23 08.711 ± 0.021	(0.605 ± 0.056) × (0.389 ± 0.036)	10.5	184 ± 15
	F1	17 47 20.125 ± 0.053	-28 23 03.920 ± 0.062	(1.050 ± 0.170) × (0.680 ± 0.110)	144.0	1090 ± 170
	F2	17 47 20.167 ± 0.014	-28 23 03.588 ± 0.012	(0.316 ± 0.047) × (0.204 ± 0.060)	82.0	124 ± 15
	F3a	17 47 20.155 ± 0.012	-28 23 04.878 ± 0.016	(0.203 ± 0.061) × (0.129 ± 0.090)	64.0	34 ± 6
	F3cd	17 47 20.180 ± 0.014	-28 23 04.628 ± 0.015	(0.478 ± 0.054) × (0.445 ± 0.057)	118.0	518 ± 39
	F3e	17 47 20.219 ± 0.006	-28 23 04.582 ± 0.013	(0.206 ± 0.049) × (0.145 ± 0.030)	1.0	32 ± 4
	F4	17 47 20.218 ± 0.005	-28 23 04.205 ± 0.007	(0.243 ± 0.029) × (0.180 ± 0.032)	123.0	105 ± 7
	F10.27	17 47 20.081 ± 0.003	-28 23 05.220 ± 0.011	(~0.22) × (~0.08)		3 ± 0.6
	F10.37	17 47 20.182 ± 0.003	-28 23 05.797 ± 0.005	(0.151 ± 0.018) × (0.050 ± 0.044)	103.0	30 ± 2
	F10.39	17 47 20.197 ± 0.001	-28 23 06.484 ± 0.004	(~0.078) × (~0.055)		12 ± 1
	G	17 47 20.290 ± 0.014	-28 23 02.936 ± 0.015	(0.333 ± 0.055) × (0.179 ± 0.067)	55.0	93 ± 13
	I	17 47 20.385 ± 0.064	-28 23 05.167 ± 0.071	(3.88 ± 0.20) × (1.293 ± 0.10)	40.1	3740 ± 190
	I10.52	17 47 20.332 ± 0.006	-28 23 08.006 ± 0.013	(~0.140) × (~0.093)		8 ± 2
	K1	17 47 19.781 ± 0.009	-28 22 20.588 ± 0.022	(0.612 ± 0.056) × (0.285 ± 0.026)	8.9	123 ± 10
	K2	17 47 19.883 ± 0.002	-28 22 18.412 ± 0.007	(0.424 ± 0.018) × (0.088 ± 0.003)	164.1	32 ± 1
	K3	17 47 19.903 ± 0.013	-28 22 17.051 ± 0.014	(0.442 ± 0.054) × (0.429 ± 0.056)	129.0	181 ± 13
	K4	17 47 20.017 ± 0.015	-28 22 04.474 ± 0.020	(1.196 ± 0.049) × (0.848 ± 0.034)	159.8	289 ± 12
	K7	17 47 19.905 ± 0.008	-28 22 13.401 ± 0.027	(0.347 ± 0.081) × (0.104 ± 0.018)	166.2	7 ± 1
	Z10.24	17 47 20.043 ± 0.001	-28 22 41.143 ± 0.003	(0.175 ± 0.013) × (0.111 ± 0.007)	147.9	23 ± 1
	S	17 47 20.472 ± 0.041	-28 23 45.120 ± 0.034	(1.747 ± 0.113) × (0.840 ± 0.057)	54.0	1231 ± 79



**Table B.6.** NH<sub>3</sub> maser positions in Sgr B2, derived from the JVLA observations.

Transition		R.A.	Dec.	$S_\nu$	$T_{\text{MB}}$	$V_{\text{LSR}}$	$\Delta V_{1/2}$
		( <i>h m s</i> )	( $^\circ$ ' ")	(Jy beam <sup>-1</sup> )	(10 <sup>4</sup> K)	(km s <sup>-1</sup> )	
(6,3)	63A <sup>+</sup>	17 47 20.005 ± 0.003	-28 22 17.285 ± 0.009	0.058	1.026	62.09 ± 0.02	0.60 ± 0.04
	63B <sup>+</sup>	17 47 19.918 ± 0.002	-28 22 17.037 ± 0.008	0.085	1.503	68.94 ± 0.01	0.40 ± 0.02
	63C <sup>x</sup>	17 47 20.036 ± 0.001	-28 22 41.135 ± 0.004	0.114	2.028	57.26 ± 0.01	0.49 ± 0.01
	63D <sup>*</sup>	17 47 20.200 ± 0.002	-28 23 06.500 ± 0.008	0.019	0.345	69.02 ± 0.12	1.14 ± 0.12
				0.048	0.850	70.22 ± 0.12	0.62 ± 0.12
				0.027	0.470	71.00 ± 0.12	0.48 ± 0.12
				0.098	1.720	71.80 ± 0.12	0.44 ± 0.12
(7,4)	74A <sup>+</sup>	17 47 20.005 ± 0.001	-28 22 17.255 ± 0.002	0.381	6.771	62.58 ± 0.002	0.37 ± 0.005
	74B <sup>*</sup>	17 47 20.200 ± 0.001	-28 23 06.512 ± 0.005	0.125	2.219	72.55 ± 0.006	0.72 ± 0.02
	74C <sup>**</sup>	17 47 20.471 ± 0.001	-28 23 45.783 ± 0.005	0.177	3.144	77.41 ± 0.004	0.54 ± 0.01
	85A <sup>+</sup>	17 47 19.862 ± 0.003	-28 22 18.254 ± 0.011	0.019	0.340	54.32 ± 0.06	0.88 ± 0.17
(9,6)	85B <sup>*</sup>	17 47 20.118 ± 0.005	-28 23 06.230 ± 0.015	0.024	0.444	70.95 ± 0.04	0.95 ± 0.08
	96A <sup>+</sup>	17 47 19.876 ± 0.002	-28 22 17.903 ± 0.009	0.070	1.207	77.92 ± 0.02	0.94 ± 0.05
	96B <sup>+</sup>	17 47 19.855 ± 0.003	-28 22 17.977 ± 0.010	0.083	1.416	63.78 ± 0.01	0.82 ± 0.03
	96C <sup>*</sup>	17 47 20.200 ± 0.001	-28 23 06.511 ± 0.005	0.217	3.712	71.24 ± 0.13	0.73 ± 0.13
				3.211	55.15	72.48 ± 0.13	0.56 ± 0.13
				1.208	20.59	73.24 ± 0.13	0.59 ± 0.13
	96D <sup>**</sup>	17 47 20.471 ± 0.002	-28 23 45.763 ± 0.008	0.172	3.214	77.38 ± 0.01	0.66 ± 0.03
				0.066	1.097	78.20 ± 0.09	1.27 ± 0.14
				0.079	1.378	82.60 ± 0.01	0.81 ± 0.03
				0.064	1.086	83.52 ± 0.01	0.90 ± 0.06
(10,7)	107A <sup>+</sup>	17 47 19.859 ± 0.002	-28 22 12.925 ± 0.010	0.069	1.257	65.55 ± 0.02	0.57 ± 0.04
	107B <sup>+</sup>	17 47 19.259 ± 0.001	-28 22 14.724 ± 0.003	3.710	67.17	81.98 ± 0.001	0.96 ± 0.002
				0.263	4.770	86.35 ± 0.01	0.60 ± 0.02
	107C <sup>+</sup>	17 47 19.862 ± 0.003	-28 22 18.257 ± 0.011	0.041	0.751	55.08 ± 0.03	1.39 ± 0.10
				0.029	0.520	56.36 ± 0.03	0.46 ± 0.07
				0.053	0.961	57.24 ± 0.03	1.21 ± 0.09
	107D <sup>*</sup>	17 47 20.117 ± 0.002	-28 23 06.216 ± 0.006	0.165	2.967	69.48 ± 0.13	0.72 ± 0.13
			0.139	2.706	70.23 ± 0.13	0.61 ± 0.13	
			0.137	2.446	70.89 ± 0.13	0.69 ± 0.13	
107E <sup>**</sup>	17 47 20.471 ± 0.002	-28 23 45.779 ± 0.007	0.123	2.224	78.42 ± 0.01	1.25 ± 0.02	

**Notes.** <sup>(+)</sup> These nine maser spots originate in Sgr B2(N). <sup>(x)</sup> 63C arises in Sgr B2(NS). <sup>(\*)</sup> These five maser sources belong to Sgr B2(M). <sup>(\*\*)</sup> These three maser spots originate in Sgr B2(S). The flux density scale calibration accuracy is estimated to be within 15%.